1993ApJ...413..571S

THE ASTROPHYSICAL JOURNAL, 413:571–581, 1993 August 20

FRAGMENTATION AND KINEMATICS OF THE W49N CLOUD CORE

E. SERABYN,[1] R. GÜSTEN,[2] AND A. SCHULZ[3]

Received 1992 November 13; accepted 1993 March 3

ABSTRACT

A multitransitional study of the W49N molecular cloud core has been carried out in seven rotational lines of CS and $C^{34}S$, ranging in excitation from $J = 3\text{–}2$ to $J = 10\text{–}9$. The cloud core has been found to consist primarily of three dense molecular clumps, of size 0.4–1.0 pc, located approximately along an axis at P.A. 56° on the plane of the sky. The clumps' local densities are $2\text{–}6 \times 10^6$ cm^{-3}, and their masses a few 10^4 $M_\odot$ each, yielding a total core mass of $\approx 10^5$ $M_\odot$. The two outer clumps are receding from us at an LSR velocity of 12 km s^{-1}, but the central clump is instead moving away at only 4 km s^{-1}, indicating that two different molecular clouds are present toward W49A. Absorption studies place the 12 km s^{-1} gas closer to us than the 4 km s^{-1} gas, implying that these two molecular clouds are converging upon each other. In addition, the central CS clump is found to be spinning rapidly (with a gradient of 3 km s^{-1} pc^{-1}) in a direction counter both to Galactic rotation, and to the direction inferred earlier from recombination line observations of the W49A compact H II regions. The hypothesis of global molecular cloud collapse, which was inferred for W49N from the recombination line observations, is thus found to be inconsistent with our new molecular line data. Instead, the molecular gas kinematics suggest that the enhanced O-star formation rate in W49N has been triggered by a cloud-cloud collision, which we hypothesize has resulted from orbit crowding in our Galaxy's Sagittarius spiral arm.

Subject headings: ISM: individual (W49) — ISM: kinematics and dynamics — ISM: molecules — radio lines: ISM — stars: formation

1. INTRODUCTION

The W49A molecular cloud is one of the most luminous and massive star-forming complexes in our Galaxy. Located on the opposite side of the Galaxy, 11.4 kpc hence (Gwinn, Moran, & Reid 1992), it contains several 10^5 $M_\odot$ of molecular gas (Scoville & Solomon 1973; Mufson & Liszt 1977; Miyawaki, Hayashi, & Hasegawa 1986), generates a total luminosity in excess of 10^7 $L_\odot$ (Ward-Thompson & Robson 1990; Sievers et al. 1991) and contains the brightest H_2O maser cluster in our Galaxy (Walker, Matsakis, & Garcia-Barreto 1982; Gwinn et al. 1992). Interestingly, the radio continuum emission from W49A has been found to arise in a dozen or so compact H II regions (Dreher et al. 1984; Welch et al. 1987; Dickel & Goss 1990), the locations and velocities of which are suggestive of a ring of H II regions in rotation about a massive cloud center (Welch et al. 1987).

We begin with a brief review of the source nomenclature. W49 consists of two main components, the molecular cloud/H II region complex W49A, and an unrelated supernova remnant W49B, located 12′ to its east (Mezger, Schraml, & Terzian 1967; Wilson 1975; Clegg, Rowan-Robinson, & Ade 1976). W49A itself shows three main subcomponents at far-infrared wavelengths, W49NW, SE & SW (Harvey, Campbell, & Hoffman 1977), of which the brightest, W49NW, is normally referred to as W49N (e.g., Dreher et al. 1984; Gordon & Jewell 1987; Schloerb, Snell, & Schwartz 1987; Ward-Thompson & Robson 1990; Sievers et al. 1991). However, the name W49A has occasionally also been applied to the main cloud peak itself (e.g., Welch et al. 1987; Keto, Lattanzio, & Monaghan 1991). In keeping with the predominant usage, we use W49N to refer to the main cloud peak in the following, reserving W49A to refer to the entire molecular cloud.

Because of its great distance, high spatial resolution observations of the dense molecular gas associated with W49A are rather sparse. Low excitation lines of CO and CS have been mapped at moderate resolution (Mufson & Liszt 1977; Phillips et al. 1981; Miyawaki et al. 1986, Schloerb, Snell, & Schwartz 1987), but otherwise, the dense cloud core has been studied primarily in rather indirect ways. These include interferometric HCO^+ observations, which show a complex mixture of absorption and emission (Welch et al. 1987), and H_2CO absorption-line observations (Goss & Tilanus 1985; Dickel & Goss 1990), which trace only gas in front of the compact H II regions. Nevertheless, because of the interest provoked by its high O-star formation rate, and the suggestive arrangement of its H II regions, several models for the kinematics of the molecular and ionized material in W49N have been advanced, among them being a two-cloud collision scenario (Mufson & Liszt 1977; Miyawaki et al. 1986), global collapse of a massive molecular cloud (Welch et al. 1987), and fragmentation of a spinning molecular ring into individual collapsing centers (Lattanzio, Keto, & Monaghan 1991; Keto, Lattanzio, & Monaghan 1991).

To study the distribution, density, and kinematics of the molecular material in W49N in further detail, multitransitional observations of the CS and $C^{34}S$ emission from this cloud core were undertaken. W49N was mapped in three excited rotational transitions of $C^{32}S$ (hereafter CS) and two corresponding transitions of $C^{34}S$. In addition, single spectra of the highly excited CS and $C^{34}S$ $J = 10\text{–}9$ transitions were acquired toward the cloud peak (Hauschildt et al. 1993). To obtain the highest possible single-dish resolution, the three lower frequency transitions of CS and $C^{34}S$ were observed with the

---

[1] California Institute of Technology, 320-47, Pasadena, CA 91125.

[2] Max-Planck-Institut für Radioastronomie, Auf dem Hügel 69, 5300 Bonn 1, Germany.

[3] I. Physik. Institut der Universität zu Köln, Zülpicherstr. 77, 5000 Köln 1, Germany.

1993ApJ...413..571S

TABLE 1

OBSERVING PARAMETERS

Telescope	Transition	Frequency (GHz)	Observation Date	Beam	Efficiency η_{mb}	T_{rec}(DSB) (K)	Backend Spectrometer	Channel Width (km s^{-1})
IRAM 30 m.......	H35α	147.0469	1989 May	17″	0.55	150	Filterbank	2.0
	C^{32}S 3–2	146.9690	1989 May	17	0.55	150	Filterbank	2.0
	C^{34}S 5–4	241.0162	1989 May	12	0.4	250	Filterbank	1.2
	C^{32}S 5–4	244.9356	1989 May	12	0.4	250	Filterbank	1.2
	SO$_2$ $18_{1,17}$–$18_{0,17}$	240.9428	1989 May	12	0.4	250	Filterbank	1.2
CSO 10.4 m.......	C^{34}S 7–6	337.3966	1989 Sep	20	0.5	200	AOS	0.43
	C^{32}S 7–6	342.8829	1989 Sep	20	0.5	200	AOS	0.43
	C^{34}S 10–9	481.9159	1992 Apr	15	0.4	200	AOS	1.3
	C^{32}S 10–9	489.7510	1992 Apr	15	0.4	200	AOS	1.3

IRAM 30 m telescope, and the four higher frequency transitions with the Caltech Submillimeter Observatory, with beam sizes ranging from 12″ to 20″. In addition, maps in the H35α recombination line and the SO$_2$ $18_{1,17}$–$18_{0,18}$ line were acquired simultaneously with the CS observations. All observations used facility SIS receivers and backend spectrometers. A complete list of the lines observed, as well as the other observing parameters, is given in Table 1. Preliminary results have been presented in Serabyn & Güsten (1991), and further details of the observing and calibration procedures can be found in Schulz et al. (1991). The use of CS as a density probe is discussed in Snell et al. (1984) and Mundy et al. (1986).

2. RESULTS

2.1. CS *Maps*

Integrated line maps in the five CS and C^{34}S transitions surveyed are shown in Figure 1. Also indicated are the positions observed. The nominal map center is at $(\alpha, \delta) = (19^h07^m50^s, 09°01'20'')$, from which all offsets in this paper are given in arcseconds. The pointing accuracy was $\approx 3''$. All of the molecular maps in Figure 1 peak just to the right of the map center, at an average offset of about (−9, −2), although the highest resolution maps, those of the CS and C^{34}S $J = 5$–4 lines, show that the best peak location is actually at an offset of about (−6, −2). These maps also show that the molecular emission is extended NE-SW, at a position angle of ~55°. The CS emission thus bears a striking similarity to the core of the 870 μm dust continuum map of W49N (Sievers et al. 1991), both in morphology and peak position.

As delineated by the H35α transition in Figure 1, the ionized gas peaks in a different location, ~3″ directly below the nominal map center. Since the H35α line was measured simultaneously with the CS 3–2 line, these two maps have the same pointing, implying that this shift in peak position between the ionized and molecular gas components is real. The location of our H35α peak is quite close to the millimeter-wave continuum peak of Welch et al. (1987), which coincides with the brightest H II region, G (for H II region nomenclature, see Fig. 5, or Dickel and Goss 1990). However, because of the low resolution of the H35α data (compared to the interferometric H76α data of Welch et al. 1987), the H35α data provides little new information beyond this pointing check.

Figure 2 shows the CS and C^{34}S spectra obtained toward three of our positions, at offsets of (12, 12), (0, 0) and (−12, −6). The plotted CS 7–6 and C^{34}S 7–6 spectra are as observed in their 20″ sized beams, but for the other lines, the observed

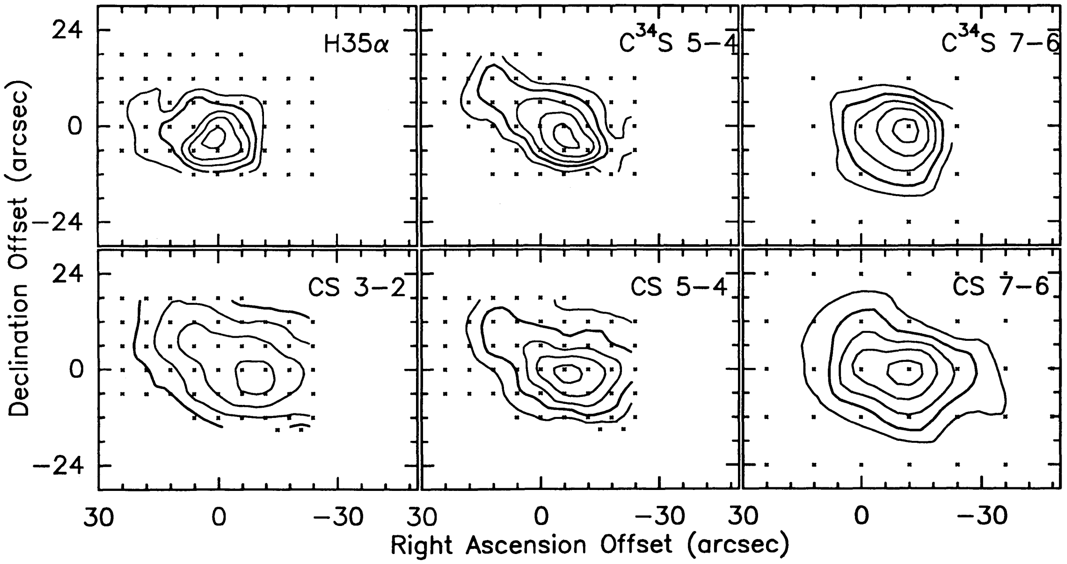

FIG. 1.—Integrated intensity contour plots of the three CS and two C^{34}S rotational transitions mapped, as well as of the H35α recombination line. The (0, 0) position is at $(\alpha, \delta) = (19^h07^m50^s.0, 09°01'20'')$, and the velocity range is −5 to 25 km s^{-1} for all lines. The beam sizes, left to right, are 17″, 12″, and 20″, respectively. The contour levels are at 35%, 50%, 65%, 80%, and 95% of the respective peaks, which are, clockwise from the top left, 40, 36, 18, 130, 250, and 190 K km s^{-1}. The heavier contours are at the 50% level.

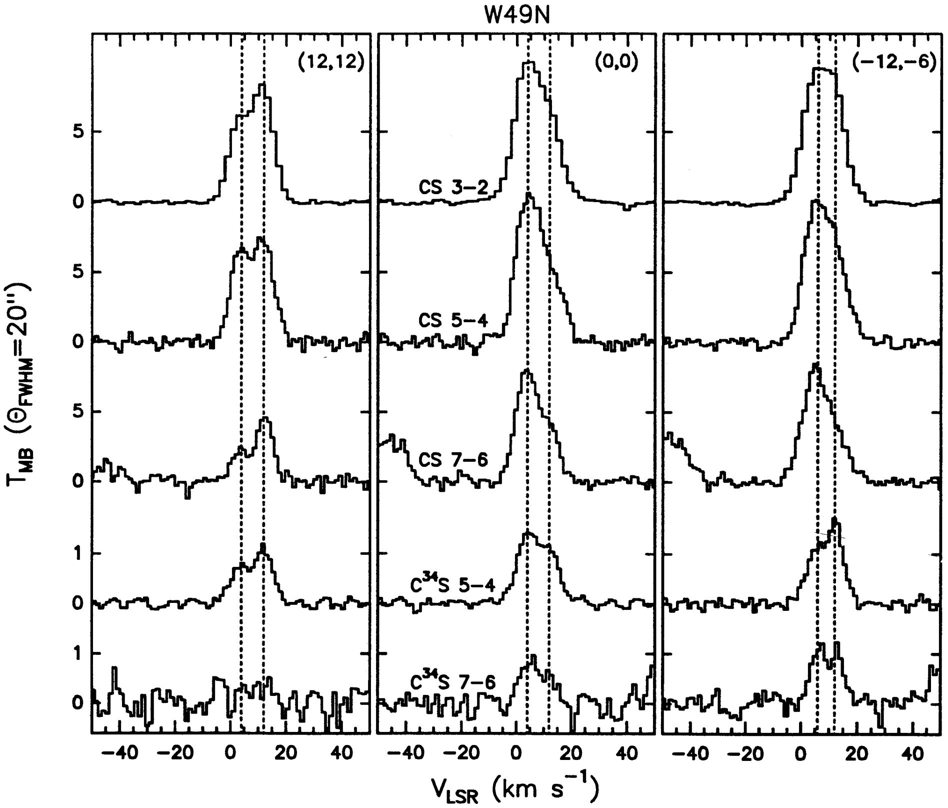

FIG. 2.—Spectra of the CS and $C^{34}S$ transitions observed toward three offset positions, all convolved to an effective observing beam of 20″. The dotted vertical lines are at 12 km s^{-1} (*all panels*), 4 km s^{-1} (*left and center panels*), and 6 km s^{-1} (*right panel*).

grid of higher resolution spectra were first numerically convolved to generate the spectra expected in the same 20″ sized observing beam. All of the lines detected show evidence for two emission components, at ∼4 and 12 km s^{-1}, but these components are particularly evident in the $C^{34}S$ 5–4 spectra, and at offset (12, 12). The relative strengths of these components vary with both rotational quantum number, J, and spatial offset, but both components clearly contribute to all of the spectra. The line widths of the individual components, determined from Gaussian fits to the line profiles, are ≈8 km s^{-1}. These two velocity components have been seen previously in lower excitation CO and CS transitions and have led to the suggestion that W49N represents the interaction of two separate clouds (Mufson & Liszt 1977; Miyawaki et al. 1986). On the other hand, because of the possibility of self-absorption in low-excitation lines, it has also been argued that the double-peaked CO line shape is determined by self-absorption in a single cloud component (Phillips et al. 1981). However, since the two velocity-component line shape is seen in all of the high-excitation transitions observed in this study, including the (presumably) optically thin $C^{34}S$ lines, and also in the very high excitation CO 7–6 line (Jaffe, Harris, & Genzel 1987), it is clear that multiple clouds at different velocities are indeed present toward W49N. This is not unexpected, as giant molecular clouds are frequently composed of many subcondensations, and at the distance of W49N, several such condensations may be present in a small projected area (1 pc = 18″ at a distance of 11.4 kpc).

In addition to the line shapes, the observed elongation of the emitting areas to the northeast seen in the highest resolution maps in Figure 1 (those of CS and $C^{34}S$ 5–4) indicates the presence of multiple subclouds. To investigate the nature of this clumping further, channel maps of the (likely) optically thin $C^{34}S$ 5–4 emission are shown in Figure 3. Three clumps are seen to predominate, the locations of which are indicated on the panels: (1) A cloud with a central velocity of ≈12 km s^{-1} is seen in the southwest, at an offset of approximately (−10, −5). The location of this cloud is the same in the 8–16 km s^{-1} channel maps, implying no large velocity gradient is present. (2) A cloud with an average velocity of ∼4 km s^{-1} peaks very close to the center of the map, at (0, 2). A rapid velocity gradient is present across this cloud, which can be traced from 0 to ∼8 km s^{-1} (east to west). Above v_{LSR} = 6 km s^{-1} however, this cloud becomes blended with the first cloud mentioned. (3) A more isolated cloud is located near the north-easterly offset of (13, 11), again with an average velocity of ∼12 km s^{-1}. This clouds also has an E-W gradient in velocity. For ease in identification, these three cloudlets will be referred to as CS-SW, CS-C, and CS-NE, respectively. The 10 km s^{-1} channel suggests the possibility that both of the clouds at 12 km s^{-1}, CS-NE and CS-SW, might be individual condensations in a more elongated filamentary structure. A realistic model for W49N is thus seen to be an agglomeration of several massive molecular subclouds, which are seen close together in projection because of their large distance from us. Although we see only three clumps in the field mapped, doubtless additional clumps exist outside this field, as attested by more distant structures seen in, e.g., H_2CO (Goss & Tilanus 1985).

Although the three clumps discussed are relatively well separated in both position and velocity, and so are reasonably

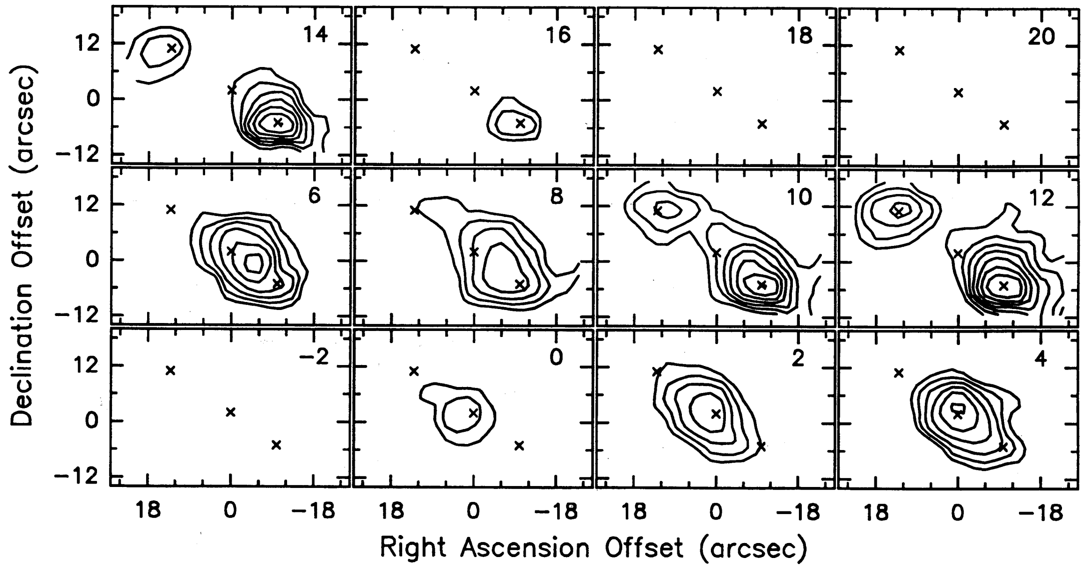

FIG. 3.—Velocity channel maps of the C ^{34}S 5–4 transition. The channels are centered at the velocities shown in the upper right corners of the panels, and spaced by 2 km s^{-1}. The levels are at 2, 2.5, 3, ... K km s^{-1}. The three crosses in each panel are reference marks located near the peaks of the three clumps, CS-NE at (13, 11), CS-C at (0, 2), and CS-SW at (−10, −5).

straightforward to identify, the nature of the clumping in the observed field was also verified with the aid of the clump deconvolution software described by Stutzki & Güsten (1990). Upon application to the C ^{34}S 5–4 data, these and only these same three clumps were found above the noise level (0.23 K). The derived clump parameters are given in Table 2, and so far as position and velocity are concerned, differ only slightly from the eyeball estimates. The deconvolved clump diameters for CS-SW and CS-NE, assuming Gaussian sources and beams, are ≈10″, or 0.55 pc. CS-C is decidely nonspherical, however, with a deconvolved size of ≈0.4 × 1 pc. This suggests that a modest increase in spatial resolution could resolve the emission from these three clumps.

The spatial location of these three clouds can be seen more clearly in the top panel of Figure 4, which superposes the 4 and 12 km s^{-1} C ^{34}S 5–4 channel maps. The three clumps are seen to line up approximately along an axis at P.A. = 56°, passing through the point (0, 2). In Figure 5*a*, these same 4 and 12 km s^{-1} channel maps are superposed on a VLA map of the W49N compact H II regions (from Dickel & Goss 1990). In this figure, the contours delineating the three molecular clumps are *not* on the same linear scale; rather, for each of the three clumps, their respective 60% and 80% contour levels are shown. The central CS-C clump at 4 km s^{-1} is seen to be well centered within the encircling H II regions B–J, while the CS-SW clump at 12 km s^{-1} is well centered on the H II region A. Since these two clouds are so close in projected distance, the velocity-integrated CS emission peaks between these two clumps (Fig. 1), at an offset of roughly (−6, −2), as does the submillimeter-wave dust continuum emission (Sievers et al. 1991). The third clump, CS-NE, is not cleanly centered on any ionized structure, but is partially surrounded by the H II regions K, L and M. The submillimeter dust continuum emission is also extended toward this clump (Sievers et al. 1991). The projected locations of the CS clumps on the radio continuum map, together with their rather large deconvolved clump sizes discussed above, thus suggest that the deconvolved molecular cloud structure consists not of a host of individual clumplets associated individually with each of the compact H II regions, but rather of only a few, more massive, and "centrally located," condensations, corresponding to the three CS clumps.

2.2. *Comparison with Other Data*

A position-velocity diagram along the clump "major axis" described above is shown in Figure 6, in which the three CS clumps are clearly evident as three separate spatial and kinemetic features. In this orientation, CS-C is a bit more extended than the other clumps and shows the only significant velocity gradient. The position-velocity plot indicates that CS-C is likely rotating, with a gradient of ≈3 km s^{-1} pc^{-1}, in agreement with the clump fitting results (Table 2). The angular momentum vector of this rapidly rotating clump is nearly opposite in direction to the angular rotation of the Galaxy itself. Surprisingly, the direction of rotation of CS-C is also *opposite* to that inferred from the velocities of the H76α recombination lines arising in the compact H II regions (Welch et al.

TABLE 2

OBSERVED CLUMP PARAMETERS

Clump	($\Delta\alpha$, $\Delta\delta$) Centroid	Observed FWHM	Major Axis P.A.	Deconvolved FWHM	V_{LSR} (km s^{-1})	ΔV_{FWHM} (km s^{-1})	$\lvert\nabla V\rvert$ (km s^{-1} arcsec^{-1})	P.A. of ∇V
CS-NE	(14″0, 11″6)	15″2 × 15″7	34°	9″ × 10″	11.9	6.2	0.15	103°
CS-C	(0.6, 3.4)	14.0 × 21.3	62	7 × 18	4.3	8.2	0.15	−91
CS-SW	(−9.3, −3.2)	15.5 × 15.6	44	10 × 10	11.5	8.1	0.04	106

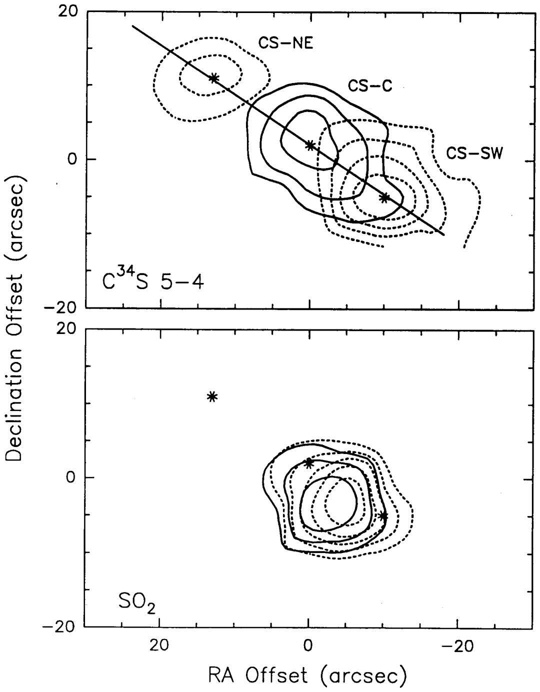

FIG. 4.—Superposition of the 4 km s^{-1} (*solid lines*) and 12 km s^{-1} (*dotted lines*) velocity channels (2 km s^{-1} wide) of the C^{34}S 5–4 (*top panel*) and SO$_2$ $18_{1,17}$–$18_{0,17}$ (*bottom panel*) emission. The three asterisks mark the peaks of the three C^{34}S 5–4 clumps. The line oriented at 56° passing through the three clumps is referred to in the text as the clump "major axis." The contour levels for the C^{34}S 5–4 map are at 45%, 60%, 75%, and 90% of the peak level of 5.6 K km s^{-1}, and for the SO$_2$ map, 30%, 45%, 60%, 75%, and 90% of the peak level of 10 K km s^{-1}.

1987). Based on H_2CO absorption data, and the velocities of the OH masers (from Johnston & Hansen 1982 and Gaume & Mutel 1987) located near the compact H II regions B and G, Dickel & Goss (1990) had also noted an incongruity between the molecular and ionized velocities. As we now discuss, the CS results are able to provide for a ready understanding of this discrepancy. Thus, for ease in comparison to the H76α and H_2CO velocities, these data have been superposed on the C^{34}S position-velocity plot, by projecting the H II region locations onto the 56° axis running through the three CS clumps. The H76α velocities are from Table 2 in Dickel & Goss (1990), and the H_2CO absorption FWHM's from their Figure 1.

The contrast between the molecular and ionized velocities in Figure 6 is striking. While the central velocity of CS-C is seen to blueshift toward higher offsets (the offsets being in the same sense as α offsets), the H II regions B–K, upon which the rotation curve of Figure 2 in Welch et al. (1987) is based, tend to redshift toward higher α. As Figure 6 suggests, this is likely due to the fact that each of the H II regions is associated not with a single overall flow pattern, but rather with a number of different molecular clumps, each with its own systemic velocity. However, because H II regions can have large-scale internal motions, a direct association of the compact H II regions with the molecular clumps, based only on the H76α velocities, is not feasible. In addition, as Welch & Marr (1987) had already earlier pointed out for the case of W3OH, the optical depth through compact H II regions in centimeter wave recombination lines can be large, and so the velocities derived from these transitions are likely not reliable tracers of the overall gas kinematics. Thus, since the measured H76α velocities of the W49N compact H II regions do not reflect the molecular kinematics, the conclusion must be that these velocities do not reflect the gravitational potential, and so provide no information on the mass distribution in the W49A cloud.

However, comparing the velocities of the CS clumps with the H_2CO absorption and OH and H_2O maser velocities, it is possible to uniquely assign most of the compact H II regions to individual CS clumps, and also to reconstruct the relative locations of most of the gas components along the line of sight. First we note that all previous absorption line studies, of both the H_2CO and HCO^+ molecules (see § 4 below; Scoville & Solomon 1973; Fomalont & Weliachew 1973; Goss & Tilanus 1985; Welch et al. 1987), have unanimously concluded that the 4 km s^{-1} gas lies behind the 12 km s^{-1} gas. Thus, since only the centralmost H II regions C, F, and G have significant H_2CO absorption at or near 4 km s^{-1}, these three must be assigned to clump CS-C. For G, its associated OH masers show a range of 2–8 km s^{-1}, confirming this assignment. In addition, the H_2O masers near component G show evidence for overall rotation in the same sense as the CS-C clump (Gwinn et al. 1992). Of these three H II regions, only the most northeasterly, F, shows no absorption at 12 km s^{-1}. This is consistent with the 4 km s^{-1} CS-C gas being located both behind and to the side (northeast) of the 12 km s^{-1} CS-SW gas, so that in projection, F lies beyond the edge of CS-SW, but C and G do not (see Fig. 5).

In the southwest, components A, B, and D show strong H_2CO absorption only from the 12 km s^{-1} component, and for component B, the OH maser velocities lie in the range 7–21 km s^{-1}. Based on this agreement in velocity with the 12 km s^{-1} CS component, all three of these H II regions are likely associated with CS-SW. The lack of 4 km s^{-1} absorption toward all three of these components again implies that CS-C is behind CS-SW. (Thus, from our vantage point on Earth, the clumps are properly oriented front to back if we look at the position velocity diagram from the right-hand side.) Note that several of the above assignments (B, D, and G) are either contrary to what H76α velocities alone suggest, or are ambiguous solely on that basis (F). Finally, in the northeastern region of the map, the H II regions, L and M show H_2CO absorptions consistent with an association with CS-NE, while J is too weak to be certain. For I and K, we have no H_2CO data, and so are forced to rely on the H76α information, which suggests an association with CS-NE, or with the weak 12 km s^{-1} emission connecting CS-NE and CS-SW. Thus, *all* available molecular velocity information is consistent with the tripartite clumping of the molecular gas found in W49N.

2.3. SO_2 *Emission*

The SO_2 $18_{1,17}$–$18_{0,17}$ line, which shared a sideband with the C^{34}S 5–4 line, was mapped simultaneously with the latter line, yielding maps in the two lines with identical pointing. The SO_2 spectra show contributions from the same two velocity components as CS and C^{34}S, but, as Figure 4 reveals, the SO_2 emitting region is much more compact. Figure 4, which compares the C^{34}S 5–4 and SO_2 emission in both the 4 and 12 km s^{-1} velocity bins, shows that the SO_2 emission is practically unresolved (except for weak emission at the 10% level which does not appear on the map, but which does extend further). Indeed, both of the SO_2 velocity components peak up sharply

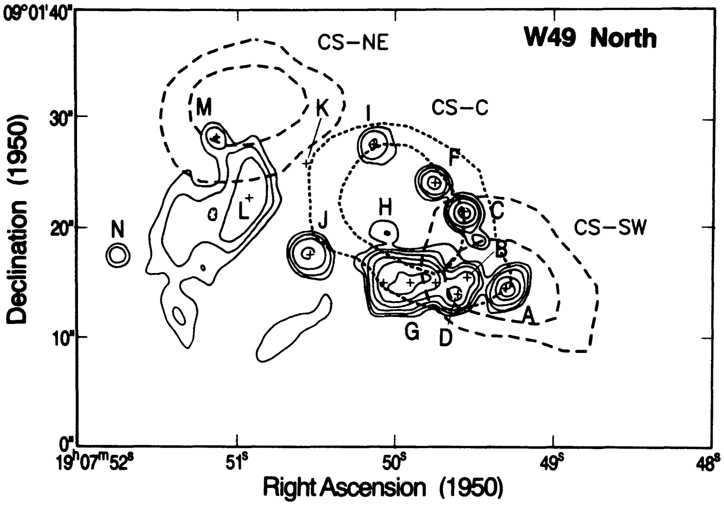

FIG. 5a

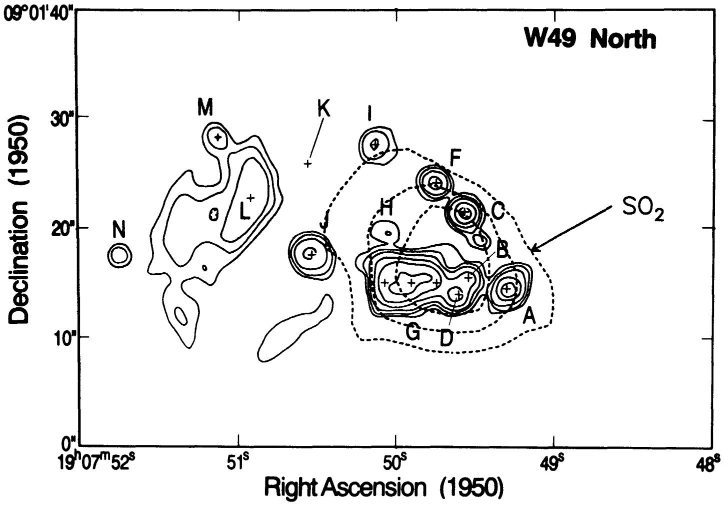

FIG. 5b

FIG. 5.—(a) Superposition of the 4 km s^{-1} (*dotted lines*) and 12 km s^{-1} (*dashed lines*) $C^{34}S$ 5–4 channel maps on the VLA 2 cm continuum map of the W49N compact H II regions (from Dickel & Goss 1990). The $C^{34}S$ 5–4 contours are at 60% and 80% of the peak levels of each of the three clumps. (b) Superposition of SO_2 integrated emission (−5 to 25 km s^{-1}) contours on the same field, with contour levels of 25%, 50%, and 75% of the peak.

at the *same* location, just *between* clumps CS-C and CS-SW. This is quite unlike the behavior of the CS lines, which show markedly different peak locations in the different velocity channels (although coincidentally, the velocity-integrated $C^{34}S$ 5–4 peak in Figure 1 agrees in location with the SO_2 maximum).

This interstitial SO_2 location, together with the high excitation energy of this transition ($E_{\rm lower} = 151.5$ K), immediately suggests a collisional shock excitation mechanism. Indeed the abundance of SO_2 is expected to be strongly enhanced in shocked gas (Pineau des Forêts et al. 1993). On the other hand, as Figure 5*b* shows, the SO_2 peak is also exactly coextensive with the region of the strongest H II regions, and so the strongly localized nature of the SO_2 emission may be due to hotter gas temperatures occuring close to the embedded heating sources, as in the core of OMC-1 (Schloerb et al. 1983; Plambeck 1988). Higher resolution observations will certainly be necessary to sort out the true nature of the SO_2 emitting region.

2.4. CS *and* $C^{34}S$ *J = 10–9 Lines*

Finally, the single spectra of the CS and $C^{34}S$ $J = 10$–9 transitions (described more fully in Hauschildt et al. 1993), observed toward the velocity-integrated cloud peak at (−6, 0), are shown in Figure 7. Also shown, for comparison, are the $C^{34}S$ 7–6 lines toward this same position, convolved and rescaled, respectively (see Fig. 7 caption), to the same 15″ beam. The CS 10–9 spectrum shows strong emission at ≈5.5 km s^{-1}, with only a weak extension to the higher velocities of the 12 km s^{-1} component. The 5.5 km s^{-1} velocity is completely consistent with emission from CS-C, if we allow for the observed E-W velocity gradient across this clump (Fig. 6).

The $C^{34}S$ 10–9 spectrum toward this position also shows the 5.5 km s^{-1} emission, but the higher velocity emission appears broader and more redshifted than in the less excited $C^{34}S$ transitions included in Figure 7. This broadening is unfortunately due to blending with a previously unlisted CH_3 OH line in the image band, at 479.128 GHz. Since the

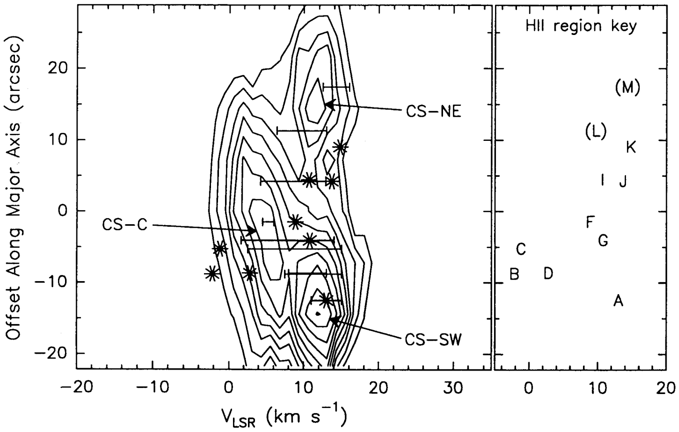

FIG. 6.—Position-velocity diagram along the major axis of the three CS clumps (see Fig. 4). H76α velocities (*asterisks*) and H_2CO absorption FWHM's (*bars*) from Dickel & Goss (1990) are superposed. The H76α data have been placed at offsets corresponding to the projected locations of the H II regions along the $C^{34}S$ major axis. The finder key on the right gives the H II region nomenclature in the same relative locations as the corresponding asterisks appear in the panel to the left. The letters in parentheses refer to H II regions for which no H76α velocities are available, and which are therefore positioned according to their H_2CO absorption velocities.

intensity of the 12 km s^{-1} component is thus difficult to fit for the $C^{34}S$ $J = 10$–9 line, we use only the main line intensity for this velocity component in the following analysis.

3. DENSITY ANALYSIS

3.1. *The LVG Model*

The presence of three molecular clumps toward W49N complicates the planned density analysis, but not greatly. We thus undertake a statistical equilibrium excitation analysis toward each of the three molecular peaks, under the large velocity gradient (LVG) assumption, as in, e.g., Schulz et al. (1991). We begin with the simplest assumption of three homogeneous clumps, although in truth, the slightly larger extent of the CS 3–2 map, compared to the higher excitation transitions, suggests that the clumps are embedded in a more extended, lower density medium. We also neglect possible radiative interactions between different clumps along the same line of sight. The CS/$C^{34}S$ abundance ratio was assumed equal to the terrestrial isotopic sulfer ratio of 23.

All of the LVG models used a gas kinetic temperature of 50 K, since this is the temperature of the most luminous dust component of W49N (Erickson & Tokunaga 1980; Ward-Thompson & Robson 1990; Sievers et al. 1991; Ward-Thompson, Berry, & Robson 1992), and a few weak CH_3CN spectra we acquired [with $T_{MB} \sim 0.3$ K for $(J, K) = (8, 2)$–$(7, 2)$] seemed consistent with this temperature. A hotter but less luminous dust component is also present (Sievers et al. 1991; Ward-Thompson, Berry, & Robson 1992), but the extremely small source size of this component (1.6 arcsec^2; Ward-Thompson et al. 1992), compared to the CS clump sizes ($\approx 10^2$ arcsec^2; see Table 2 and below) suggests that the 50 K temperature is the more relevant one for the CS emission.

For the LVG analysis, the spectra closest to the three individual clump centers were used, at offsets of $(-12, -6)$, (0, 0), and 12, 12). The first step was to normalize all spectra to the T_{MB} (main beam temperature) scale, using the beam efficiencies in Table 1. Next, the different beam sizes were taken into account by convolving the extant grid of measured spectra to simulate the spectra which would appear in the largest of the observing beams, 20″. The resultant spectra are shown in Figure 2. Two-component Gauss fits were then made to all of the line shapes, and the resultant peak T_{MB}'s are plotted in Figure 8 for both velocity components at all three locations. These peak T_{MB}'s were compared to the radiation temperatures predicted by the LVG models by scaling the model outputs with a variable area filling factor, f. For the central position, the CS and $C^{34}S$ 10–9 data are also included, as explained separately below.

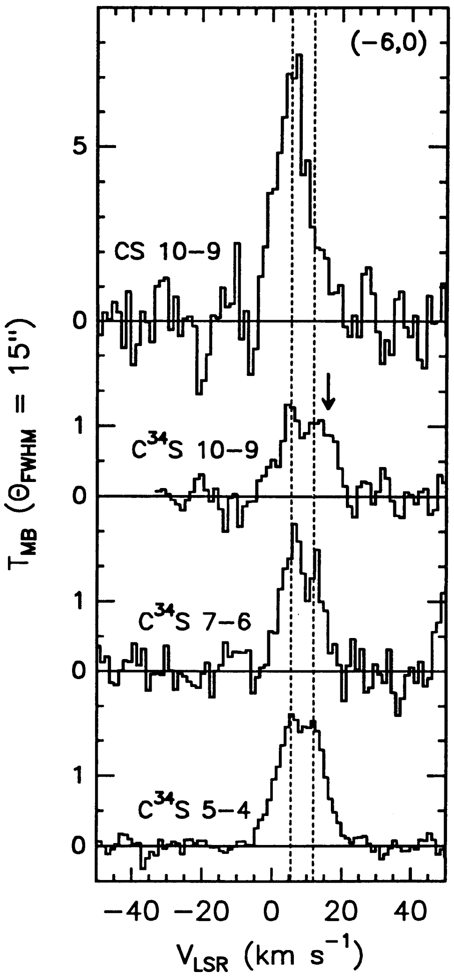

FIG. 7.—Measured CS and $C^{34}S$ $J = 10$–9 spectra toward an offset of $(-6, 0)$ in a 15″ beam. Also included are the $C^{34}S$ 5–4 and 7–6 spectra corrected to the same beam size. The former has been convolved with surrounding spectra, as described in the text, while the latter is simply rescaled, allowing for a filling factor of 0.24 in the actual 20″ observing beam, under the assumption that the beam and the clumps are symmetric and Gaussian. The dotted vertical lines are at 5.5 and 12 km s^{-1}. The arrow above the $C^{34}S$ 10–9 line gives the location of a methanol line from the image band.

3.2. *Model Results*

The results of the modeling are plotted in Figure 8. Beginning at the central position, and ignoring the $J = 10$–9 data for now, it can be seen that homogeneous LVG models can fit the brightness temperatures of all five of the lower frequency CS and $C^{34}S$ lines rather well, for both velocity components. The derived density for the 4 km s^{-1} emission from CS-C is 6×10^6 cm^{-3}, with $f = 0.24$. The line opacities are typically 0.2–0.3 for

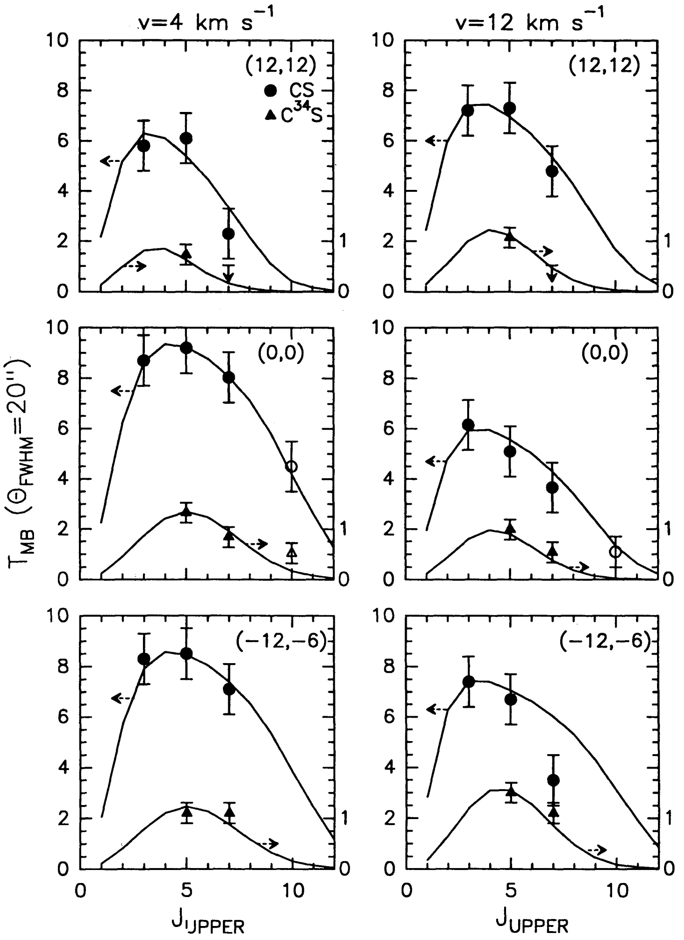

FIG. 8.—Points: T_{MB} in a 20″ beam, vs. rotational level J, for CS (*filled circles*) and C^{34}S (*filled triangles*), toward the peaks of the three molecular clumps. The left-hand column shows the results for the 4 km s^{-1} velocity component, and the right-hand column for the 12 km s^{-1} component. The dashed arrows point toward the appropriate vertical scales: the left-hand side for the CS intensities, and the right-hand side for C^{34}S. The (0, 0) panels also include, as open symbols, the CS and C^{34}S $J = 10$–9 data toward the offset (−6, 0). *Curves*: LVG model predictions for same.

the C^{34}S lines, and 3–5 for the CS lines. The other model parameters are summarized in Table 3. The same density and filling factor are also found for this velocity component in the spectra toward CS-SW, lending some additional credence to the result. However, toward CS-NW, the model fit is not nearly as good, and the density of the 4 km s^{-1} gas appears to drop. This likely is the result of being very far from the center of this clump at this location, implying that the assumption of homogeneous clumps may be an oversimplification. Nevertheless, as the fits toward the clump center indicate, the homogeneous assumption is not a bad one for this case.

As to the 12 km s^{-1} gas, the fits are both good, and similar to each other, at offsets of (12, 12) and (0, 0), with densities of 2×10^6 cm^{-3} and filling factors near 0.2 derived (Table 3). However, at (−12, −6), the fit is poorer, and one of the lines, the CS $J = 7$–6, was simply ignored (it being rather difficult to achieve such a such a low CS 7–6 to C^{34}S 7–6 ratio without at the same time making the CS 5–4 to C^{34}S 5–4 ratio comparably low). Nevertheless, a fit to the other four lines can be found with parameters very similar to those of the 12 km s^{-1} gas at the other two locations (Table 3).

The resultant filling factors and beam-averaged H$_2$ column densities are actually very similar for all three of the CS clumps (Table 3), ~0.2 and 10^{24} cm^{-2}, respectively (the latter for an assumed CS abundance of 3×10^9; Irvine et al. 1985; Blake et al. 1987). The typical filling factor of ≈0.2 in our 20″ beam yields an intrinsic linear source size of ≈10″, in very good agreement with the source sizes derived from direct deconvolution of the C^{34}S 5–4 maps (Table 2). Thus, the filling factor is apparently entirely due to the large-scale coupling of the three clumps to the beam, and not to small-scale clumping.

The derived CS column densities imply masses for the three clumps of 3–6 × 10^4 $M_\odot$ each (M_{col} in Table 3). Alternatively, the derived excitation densities and beam filling factors can be used to derive a second set of mass estimates, which are independent of the assumed CS abundance. Assuming spherical clumps of a size given by the source filling factor, the resultant "excitation density masses" (M_{exc} in Table 3) agree with the "column density masses" to better than a factor of 3. Because of uncertainties in the CS abundance (and C^{34}S/CS relative abundance; Schloerb et al. 1983; Blake et al. 1987), and clump filling factors and geometries, it is best to use the average of these two mass estimates, listed under M_{avg} in Table 3. The total cloud core mass is very similar in the two cases, the sum of the three clump masses being $\approx 1.0 \pm 0.2 \times 10^5$ $M_\odot$. This total mass is a factor of 2.5 higher than the mass estimated for the central core of W49N from dust measurements (4.1×10^4 $M_\odot$; Sievers et al. 1991), which is quite reasonable agreement, given the uncertainties in submillimeter dust opacities, the abundances of CS and C^{34}S, the homogeneous LVG assumption, and the differences in the emitting areas involved.

The velocity gradient across CS-C can also be used to estimate its mass, assuming that this gradient is due to rotation and not to the velocity shift between two even smaller, unre-

TABLE 3

CLUMP DENSITY SOLUTIONS FOR VELOCITY COMPONENTS OF 4 AND 12 km s^{-1}

Velocity Component	Offset	Volume Density n_{H_2} (10^6 cm^{-3})	Area Filling Factor f	$\langle N_{CS}/\Delta v\rangle_{beam}$ (10^{14} cm^{-2}/km s^{-1})	$\langle N_{H_2}\rangle_{beam}$ (10^{24} cm^{-2})	M_{col} (10^4 $M_\odot$)	M_{exc} (10^4 $M_\odot$)	M_{avg} (10^4 $M_\odot$)
4 km s^{-1}	(12, 12)	1	0.20	3.3	0.9	...	...	...
	(0, 0)	6	0.24	4.0	1.1	3.4	5.3	4.4
	(−12, −6)	6	0.22	4.0	1.1	...	...	...
12 km s^{-1}	(12, 12)	2	0.20	4.6	1.0	3.0	1.2	2.1
	(0, 0)	2	0.16	4.6	1.2	...	...	...
	(−12, −6)	3	0.18	6.9	1.9	5.8	1.9	3.9

solved clumps. However, here the spatial resolution is not sufficient to provide a definitive outer radius or terminal velocity. Thus, with great trepidation we estimate a kinematic mass of $\sim 2000/\sin i\ M_\odot$ for CS-C, where i is the inclination angle of the clump's rotation axis from the line of sight. This mass is up to a factor 25 lower than the two previous mass estimates, which is difficult to understand, unless the clump is rotating in a nearly face-on plane, or rotation does not dominate the clump's internal motion.

The derived CS densities of several times 10^6 cm^{-3} are about an order of magnitude higher than those given by H_2CO absorption measurements (Dickel & Goss 1990). These two sets of values can likely be reconciled in the context of a stratified medium, with the dense CS clumps embedded in a lower density "halo," as revealed by the more spatially extended emission in the lower excitation CS lines ($J = 3$–2 in Fig. 1, and $J = 2$–1 in Miyawaki et al. 1986). Since we argued earlier that small-scale clumping is not relevant, the H_2CO results imply that the H II regions must lie in the lower density outskirts of the high-density clumps. Indeed, all of the compact H II regions except A (and N, which our $C^{34}S$ 5–4 map did not cover) appear along the peripheries of the CS clumps (Fig. 5), implying that O-star formation appears to be preferentially occurring near the surfaces of the dense clumps.

3.3. CS *and* $C^{34}S$ J = *10–9 Data*

Finally, we turn to the $J = 10$–9 data available at offset (−6, 0). Neglecting the 6″ offset in position [justified because the lower J transition intensities are similar at (0, 0) and (−12, −6); see Fig. 8], we can include these CS and $C^{34}S$ 10–9 data with the lower J measurements at the (0, 0) position. Since only single spectra are available in each of the 10–9 transitions, we cannot apply the numerical convolution procedure outlined earlier to derive $T_{\rm MB}$ in our standard 20″ beam. Instead, we assume that the two-velocity components in this line have the same filling factors in a 20″ beam as the lower transitions. The resultant $T_{\rm MB}$'s are included in the central panels of Figure 8.

The resultant CS 10–9 intensities in Figure 8 are evidently consistent with our derived model parameters and so do not need to be discussed further. However, the $C^{34}S$ 10–9 emission at 4 km s^{-1} is too bright relative to the model prediction (the 12 km s^{-1} point is not included, for reasons outlined in § 2.4). This excessively strong $C^{34}S$ 10–9 emission likely reveals a yet higher density gas phase ($n \approx 10^8$ cm^{-3}), but, on the other hand, it may also result from infrared radiative excitation, as discussed by Hauschildt et al. (1993).

4. KINEMATIC MODELS

Several kinematic models for the structure of the W49N cloud core have been advanced, beginning with the "two-cloud collision" model of Mufson & Liszt (1977). This concept was based primarily on the presence of two observed velocity components, which have by now been seen toward W49 in CO (Mufson & Liszt 1977; Scoville et al. 1987; Jaffe, Harris, & Genzel 1987), H_2CO (Goss & Tilanus 1985; Dickel & Goss 1990), and CS (Miyawaki et al. 1986; this work), over scale sizes of a few arcseconds to ∼ 10′. Expanded to include the idea of multiple subclumps in two larger scale clouds, the general idea of two molecular clouds moving at different velocities appears to adequately describe a large body of the observational data. In particular, information from absorption studies of H_2CO (Scoville & Solomon 1973; Fomalont & Weliachew 1973), has been used to deduce that the more redshifted cloud at ≈12 km s^{-1} is located in front of the continuum sources, while the 4 km s^{-1} cloud is behind them. This implies that the relative motion of the two clouds is toward each other, providing the impetus for the collision suggestion of Mufson & Liszt (1977).

More recently, high-resolution VLA and Hat Creek data have been used as a basis for a different description of W49N, namely, global collapse of a single molecular cloud (Welch et al. 1987). This conjecture was based on three sets of observations: (1) a high-resolution VLA map of the W49N compact H II regions, the arrangement of which is somewhat suggestive of a partial "ring" seen in projection, (2) the velocities of H76α recombination line spectra toward the compact H II regions, which were used to argue that this "ring" of H II regions is rotating about a massive center, and (3) HCO^+ spectra from the Hat Creek interferometer, which showed a combination of emission at bluer velocities (≈4 km s^{-1}), and absorption at redder velocities (≈12 km s^{-1}). Because it is the more redshifted material that is seen in absorption, it was again evident that the more redshifted gas is located in front of the embedded continuum sources. However, in this model, this relative motion was interpreted as due to collapse motions in a single molecular cloud.

While attractive, this model is contradicted by the CS results in all three aspects. Beginning with point 2, it has already been shown in § 2 that the H76α "rotation curve" is unrelated to the actual kinematics of the molecular gas, due likely to optical depth effects and bulk motions of the ionized gas. In addition, however, as regards point 1, since the different H II regions now appear better described by associating some number of them with each of the three different molecular clumps (§ 2), the purported partial "ring" of H II regions appears actually to be an effect of projection. Finally, as regards point 3, it is known from many observations (Mufson & Liszt 1977; Goss & Tilanus 1985; Welch et al. 1987) that the 12 km s^{-1} gas is indeed located in front of the 4 km s^{-1} gas. Since in both models discussed so far, the gas components at 12 km s^{-1} and 4 km s^{-1} are then taken as moving toward each other, the real question is whether this relative motion is due to the relative motions of two separate clouds, or the motions internal to a single cloud. This question is now easy to answer, since the CS results of this paper and Miyawaki et al. (1986), and the earlier CO observations (Mufson & Liszt 1977) indicate that the 12 km s^{-1} gas is very extended spatially, with a relatively uniform velocity. Because the velocity of the 12 km s^{-1} gas does not vary as a function of position across the source, over scales ranging from 10″ in CS to almost 10′ in CO and H_2CO, it is clear that internal collapse motions are not dominant. If this were the case, the edges of the cloud should be moving at the "average" velocity of ≈8 km s^{-1}. Since the cloud edges are instead moving at the same velocity as the cloud center, we conclude that two separate clouds moving toward each other with relatively uniform velocities are indeed involved.

A third model has also recently been advanced. Keto et al. (1991) propose that the suspected partial ring of H II regions results from the fragmentation of a spinning disk via a ring instability. In this model of a collapsing, rotating cloud of gas, the material is cleared from the center by centrifugal force, and thus there is no central mass concentration predicted. Rather, gravitational collapse is expected to be localized about a number of centers corresponding to the individual H II regions. The presence or absence of a central molecular mass concentration then makes the observational distinction between this model and the Welch et al. (1987) model quite easy. However, with the high-resolution data now available, this model would appear to be ruled out, since both the dust map of Sievers et al. (1991), and the CS maps presented herein clearly show a prominent peak centered within the H II region "ring." Of course, even higher resolution observations would be desirable to settle this point in greater detail.

We are thus left with all the evidence pointing to a "two-cloud" scenario, but with modification that the two clouds are composed of several subclumps. Thus, it would be desirable to put the "two-cloud" scenario on a firmer theoretical footing. What then are the open questions? We begin with a short summary of what is known. First, the very dense molecular gas in W49N is fragmented into three clumps, two of which have an LSR velocity of 12 km s^{-1}, and the third, 4 km s^{-1}. Including information from larger scale data, these three clumps must be individual condensations in two larger clouds moving at 4 and 12 km s^{-1}, respectively. Second, the W49N compact H II regions are distributed in all three clumps mapped in CS. Third, from our viewpoint, the less redshifted (4 km s^{-1}) material is behind the 12 km s^{-1} emission, implying that these two clouds are converging. The 8 km s^{-1} relative motion of these two clouds toward each other is somewhat larger than the random dispersion of molecular cloud velocities in our Galaxy predicts ($\sigma \sim 3$–4 km s^{-1}; Clemens 1985; Scoville & Sanders 1987), but is not large enough to be excluded on this basis. Fourth, in addition to these two coherent velocity features, the low-excitation ^{13}CO 1–0 line, which is sensitive to more diffuse gas, shows emission over the entire range -5 to 20 km s^{-1}, with a median velocity near 8 km s^{-1} (Mufson & Liszt 1977), just between the velocities of the dense clumps. This diffuse gas may also be seen in absorption in the very optically thick CO 1–0 and 2–1 lines (Phillips et al. 1980). Thus, diffuse gas, with velocities of $\approx 8 \pm 10$ km s^{-1} is "in the vicinity." How it is related to the dense molecular clumps is open. Thus, the relevant questions are (1) why are the 4 and 12 km s^{-1} clouds so close together in projection and moving toward each other with so high a relative velocity? (2) How is the diffuse gas related to the dense clumps? (3) How might the 4 and 12 km s^{-1} clouds be interacting? (4) How is this interaction related to the high density and O-star formation rate seen throughout W49N? Finally, (5) why is the angular momentum vector of the rapidly rotating CS-C clump opposite in direction to the angular rotation of the Galaxy itself? Indeed, several 10^4 $M_\odot$ of gas are counterrotating, a difficult feat in a galaxy with a relatively flat rotation curve (Mestel 1966).

We suggest that all of these phenomena find a natural explanation in the interaction of this molecular material with the spiral density wave local to W49A. In the first place, the proximity of two clouds in the field of W49N can be attributed to orbit crowding, which causes an enhanced spatial density of molecular clouds near spiral arm potential minima (Levinson & Roberts 1981; Kwan & Valdex 1983). Next, since a spiral density wave can be viewed as an enhancement of the surface mass density in the Galactic disk, the perturbation to the local gravitational potential will affect the velocity field. Tangential velocities will be higher on the outside of a spiral arm than on its interior (Yuan 1969). Radially (in a galactocentric sense), the molecular material will experience a pull toward the local mass enhancement, and so clouds on the outside of the arm will be accelerated inward, and clouds on the inside will be accelerated outward. In moving toward the spiral's potential minimum, clouds on opposite sides of a spiral arm will thus appear to move toward each other. Viewed through the disk of the Galaxy toward $l \approx 45°$, a cloud on our side of the arm will be accelerated away from us slightly, and so appear redshifted with respect to the unperturbed velocity, while the material on the far side of the arm will be slightly blueshifted.

This scenario is entirely consistent with what is seen toward W49N. Assuming that the larger scale systemic velocity in the neighborhood of W49A would be ≈ 8 km s^{-1} in the absence of a density wave perturbation (as given by the diffuse ^{13}CO emission), the two dense molecular clouds are then somewhat red- and blueshifted from this systemic velocity, with the nearer cloud being the more redshifted, as required. Relative velocities of order 10–20 km s^{-1} are expected near a density wave (Yuan 1969; Shu et al. 1972; Shu, Milione, & Roberts 1973), much in excess of the cloud-cloud dispersion in the absence of the spiral perturbation. This easily accounts for the 8 km s^{-1} line-of-sight difference between the two W49N velocity components. Indeed, the 8 km s^{-1} shift might actually be though small in this context (e.g., Vogel, Kulkarni, & Scoville 1988), but the magnitude of the velocity difference depends on the separation of the clouds, an unknown quantity, and furthermore, from our viewpoint in the Galaxy, an inclination correction to the observed velocities might be necessary. Finally, the counter-rotation of the CS-C cloud also finds a natural explanation in the perturbed velocity field close to the density wave (e.g., Blitz 1991). Thus, all aspects of the molecular velocity field near W49N are consistent with the effects of molecular clouds traversing a spiral perturbation. The interaction of molecular clouds with a spiral perturbation would also naturally explain the large number of O stars produced nearly simultaneously in W49 N (Dreher et al. 1984), via the mechanism of triggered star formation (see Vogel, Kulkarni, & Scoville 1988).

However, one important question remains—how exactly is the star formation in W49N triggered during the clouds' passage through the Sagittarius spiral arm? More specifically (e.g., Elmegreen 1987), is the star formation rate enhanced because of the overall compression of material in the local minimum of the density wave potential (the hydrodynamic viewpoint), or because of an enhanced cloud-cloud collision rate resulting from the higher spatial density of molecular clouds in the arm, which is itself caused by orbit crowding near the spiral potential minimum (the ballistic viewpoint; e.g., Kwan & Valdez 1983; Scoville & Sanders 1987)?

In the hydrodynamic viewpoint, given the velocity difference between the two clouds, it is possible to conclude that the two clouds are not going through the spiral arm with the same phase, i.e., one of them is further through the perturbation than the other. They must then be well separated, and so not interacting with each other. Given our location in the Galaxy, and assuming trailing spiral arms, the cloud furthest through the pattern would be the 4 km s^{-1} cloud. It would thus be expected to be the furthest evolved, with the most prodigious ongoing star-formation rate. This does not appear to be the case, as all three CS clumps appear to be associated with a like number of compact H II regions.

On the other hand, in the ballistic viewpoint, orbit crowding, together with a normal cloud-cloud velocity dispersion, would imply that the two clouds need not be well separated, and conversely, could actually be quite close together. Indeed, it is easy to imagine that orbit crowding could have brought these two clouds close enough together to have collided, thus inducing star formation in the colliding clumps via the propagation of compressive shock waves. The fact that both the 4 and 12 km s^{-1} clumps are forming stars supports this viewpoint and suggests that cloud-cloud collisions are indeed responsible for locally enhancing the O-star formation rate in spiral arms (Kwan & Valdez 1983; Scoville, Sanders, & Clemens 1986). The shock crossing and cloud collapse time scales for the subparsec-sized fragments in W49 ($\sim 10^5$ yr) are shorter than O star evolution time scales (few 10^6 yr) and both are much shorter than the arm crossing time ($\sim 3 \times 10^7$ yr), so that individual cloud-cloud collisions occurring anywhere in the region of orbit crowding can trigger massive star formation. As a test of this hypothesis for the case of W49N, it would be useful to image with higher angular resolution a tracer of shock-excited gas, such as a vibrational line of H_2, or perhaps the SO_2 line described herein, to determine if the 4 and 12 km s^{-1} clouds are actually interacting, or are merely different clouds passing through the spiral perturbation independently.

It is also quite interesting that all of the compact H II regions in W49, except for region A, appear along the peripheries of the CS clumps (Fig. 5). Of course, the case of region A could also be explained as due to the line-of-sight projection of this H II region against the center of the CS-SW clump. Since the numerous compact H II regions in W49N are indeed still compact, it is not possible to explain this spatial effect by supposing that the newly formed stars have already freed themselves from their molecular cocoons, as could be the case with more advanced H II regions. It appears instead that the most massive stars in W49 really have formed in the outer regions of the clumps. Such a location is nicely consistent with the cloud collision scenario, which involves after all, compression and heating of gas at clump surfaces. In addition, stellar formation theory predicts the formation of massive stars in regions of higher gas temperature (Larson & Starrfield 1971; Kravchuk & Kolesnik 1989), which again suggests their formation near cloud surfaces, in postshock, but warm, gas layers (e.g., Scoville et al. 1986).

5. SUMMARY

A multitransitional study of the W49N cloud core has revealed that the molecular gas is fragmented into three very dense clumps, with local densities of 2–6 $\times 10^6$ cm^{-3}, and masses of several $10^4\ M_\odot$ each. The total mass in the three clumps making up the cloud core is $\sim 1.0 \pm 0.2 \times 10^5\ M_\odot$. Two of the clumps have a systemic velocity of 12 km s^{-1}, while the central clump, located behind the other two from our vantage point, has a velocity of 4 km s^{-1}. All other existing molecular molecular data show kinematics consistent with an origin in the motions of these three clumps. On the other hand, the velocities provided by recombination line observations of the compact H II regions are inconsistent with the molecular velocities, even suggesting a sense of rotation opposite to that seen in the molecular gas. However, based on the molecular spectra, it is possible to uniquely assign the H II regions to their parent molecular clumps, and to arrive at a consistent kinematic picture. The molecular kinematics are interpreted in the framework of two separate molecular clouds which are passing through the density wave associated with our Galaxy's Sagittarius spiral arm. The two clouds have presumably been brought close together as a result of orbit crowding in the spiral arm potential minimum and have consequently collided, yielding a burst of high-mass star formation in the shock-compressed surface layers of both parent clouds.

This work was supported by NSF grant AST 90-15755 and NATO grant 0809/87.

REFERENCES

Blake, G. A., Sutton, E. C., Masson, C. R., & Phillips, T. G. 1987, ApJ, 315, 621

Blitz, L. 1991, in The Physics of Star Formation and Early Stellar Evolution, ed. C. J. Lada & N. D. Kylafis (Dordrecht: Kluwer), 3

Clegg, P. E., Rowan-Robinson, M., & Ade, P. A. R. 1976, AJ, 81, 389

Clemens, D. P. 1985, ApJ, 295, 422

Dickel, H. R., & Goss, W. M. 1990, ApJ, 351, 189

Dreher, J. W., Johnston, K. J., Welch, W. J., & Walker, R. C. 1990, ApJ, 283, 632

Elmegreen, B. 1987, in IAU Symp. 115, Star-forming Regions, ed. M. Peimbert & J. Jugaku (Dordrecht: Reidel), 457

Erickson, E. F., & Tokunaga, A. T. 1980, ApJ, 238, 596

Fomalont, E., & Weliachew, G. 1973, ApJ, 181, 781

Gaume, R. A., & Mutel, R. L. 1987, ApJS, 65, 193

Gordon, M. A., & Jewell, P. R. 1987, ApJ, 323, 766

Goss, W. M., & Tilanus, R. P. J. 1985, MNRAS, 215, 197

Gwinn, C. R., Moran, J. M., & Reid, M. J. 1992, ApJ, 393, 149

Harvey, P. M., Campbell, M. F., & Hoffmann, W. F. 1977, ApJ, 211, 786

Hauschildt, H., Güsten, R., Phillips, T. G., Schilke, P., Serabyn, E., & Walker, C. K. 1993, A&A, in press

Irvine, W. M., Schloerb, F. P., Hjalmarson, A., & Herbst, E. 1985, in Protostars and Planets II, ed. D. C. Black & M. S. Matthews (Tucson: Univ of Arizona Press), 579

Jaffe, D. T., Harris, A. I., & Genzel, R. 1987, ApJ, 316, 231

Johnston, K. J., & Hansen, S. S. 1982, AJ, 87, 803

Keto, E. R., Lattanzio, J. C., & Monaghan, J. J. 1991, ApJ, 383, 639

Kravchuk, S. G., & Kolesnik, I. G. 1989, Astron. Nach., 310, 359

Kwan, J., & Valdez, F. 1983, ApJ, 271, 604

Larson, R. B., & Starrfield, S. 1971, A&A, 13, 190

Lattanzio, J. C., Keto, E. R., & Monaghan, J. J. 1991, in Fragmentation of Molecular Clouds and Star Formation, ed. E. Falgarone (Dordrecht: Kluwer), 449

Levinson, F. H., & Roberts, W. W. 1981, ApJ, 245, 465

Mestel, L. 1966, MNRAS, 131, 307

Mezger, P. G., Schraml, J., & Terzian, Y. 1967, 150, 807

Miyawaki, R., Hayashi, M., & Hasegawa, T. 1986, ApJ, 305, 353

Mufson, S. L., & Liszt, H. S. 1977, ApJ, 212, 664

Mundy, L., Snell, R. L., Evans, N. J. II, Goldsmith, P. F., & Bally, J. 1986, ApJ, 306, 670.

Phillips, T. G., Knapp, G. R. Huggins, P. J., Werner, M. W., Wannier, P. G., Neugebauer, G., & Ennis, D. 1981, ApJ, 245, 512

Pineau des Forêts, G., Roueff, E., Schilke, P., & Flower, D. R. 1993, MNRAS, in press

Plambeck, R. L. 1988, in Galactic and Extragalactic Star Formation, ed. R. E. Pudritz & M. Fich (Dordrecht: Kluwer), 253

Schloerb, F. P., Friberg, P., Hjalmarson, A., Höglund, B., & Irvine, W. M. 1983, ApJ, 264, 161

Schloerb, F. P., Snell, R. L., & Schwartz, P. R. 1987, ApJ, 319, 427

Schulz, A., Güsten, R., Zylka, R., & Serabyn, E. 1991, A&A, 246, 570

Scoville, N. Z., & Sanders, D. B. 1987, in Interstellar Processes, ed. D. J. Hollenbach & H. A. Thronson (Dordrecht: Reidel), 21

Scoville, N. Z., Sanders, D. B., & Clemens, D. P. 1986, ApJ, 310, L77

Scoville, N. Z., & Solomon, P. M. 1973, ApJ, 180, 31

Scoville, N. Z., Yun, M. S., Clemens, D. P., Sanders, D. B., & Waller, W. H. 1987, ApJS, 63, 821

Serabyn, E., & Güsten, R. 1991, in Fragmentation of Molecular Clouds and Star Formation, ed. E. Falgarone (Dordrecht: Kluwer), 494

Shu, F. H., Milione, V., Gebel, W., Yuan, C., Goldsmith, D. W., & Roberts, W. W. 1972, ApJ, 173, 557

Shu, F. H., Milione, V., & Roberts, W. W. 1973, ApJ, 183, 819

Sievers, A. W., Mezger, P. G., Gordon, M. A., Kreysa, E., Haslam, C. G. T., & Lemke, R. 1991, A&A, 251, 231

Snell, R. L., Mundy, L. G., Goldsmith, P. F., Evans, N. J., II, & Erickson, N. R. 1984, ApJ, 276, 625

Stutzki, J., & Güsten, R. 1990, ApJ, 356, 513

Vogel, S. N., Kulkarni, S. R., & Scoville, N. Z. 1988, Nature, 334, 402

Walker, R. C., Matsakis, D. N., & Garcia-Barreto, J. A. 1982, ApJ, 255, 128

Ward-Thompson, D., & Robson, E. I. 1990, MNRAS, 244, 458

Ward-Thompson, D., Berry, D. S., & Robson, E. I. 1992, MNRAS, 257, 180

Welch, W. J., Dreher, J. W., Jackson, J. M., Terebey, S., & Vogel, S. N. 1987, Science, 238, 1550

Welch, W. J., & Marr, J. 1987, ApJ, 317, L21

Wilson, T. L. 1975, in H II Regions and Related Topics, ed. T. L. Wilson & D. Downes (Berlin: Springer), 424

Yuan, C. 1969, ApJ, 158, 871